Electronic Supplementary Material (ESI) for Soft Matter.

Supplementary Information for "Dynamic and mechanical evolution of an oil-water interface during bacterial biofilm formation"

David P. Rivas,[1] Nathan D. Hedgecock,[1] Kathleen J. Stebe,[2] and Robert L. Leheny[1]

[1]*Department of Physics and Astronomy, Johns Hopkins University, Baltimore, MD, USA, 21218*

[2]*Department of Chemical and Biomolecular Engineering, University of Pennsylvania, Philadelphia, PA, USA, 19104*

(Dated: July 31, 2021)

I. LIST OF SUPPLEMENTARY VIDEOS

Video S1: Clip of a bright-field microscopy video of the interface between oil and a bacteria suspension at age $t_a = 1$ hr during biofilm formation. The video was taken with 20× magnification at 30 fps and 5 ms exposure time. For reference of the scale, the large spheres have a diameter of 15 μm. The DDM results at $t_a = 1$ hr in the manuscript are based on the full video, which was 28 seconds in length.

Video S2: Clip of a bright-field microscopy video of the interface between oil and a bacteria suspension at age $t_a = 7$ hrs during biofilm formation. The video was taken with 20× magnification at 30 fps and 5 ms exposure time. For reference of the scale, the large spheres have a diameter of 15 μm. The DDM results at $t_a = 7$ hrs in the manuscript are based on the full video, which was 28 seconds in length.

Video S3: Detail of a microscopy video of an oil interface of a bacteria suspension at age $t_a = 22$ hr during biofilm formation showing rotation of a 34-μm-long ferromagnetic rod in response to an applied magnetic field. The video was taken with 20× magnification at 30 fps and 3 ms exposure time. The results in Fig. 7 of the manuscript are obtained from this video.

II. RESULTS FROM ADDITIONAL PARTICLE-TRACKING EXPERIMENTS

Figure S1 displays the ensemble mean-squared displacements (MSDs) of passively moving spherical colloids at the oil interface of a bacteria suspension obtained from three trials conducted under nominally identical conditions to the trial whose results are shown in the main text. The repeated trials displayed behavior qualitatively consistent with that described in the main text in which high-mobility, diffusive or super-diffusive motion at early interface age evolved into subdiffusive motion that depended strongly on sphere size at later age. As further illustration, Fig. S2 shows the corresponding power-law exponents and the values of the MSDs at a time lag of 10 s as a function of biofilm age from the three trials.

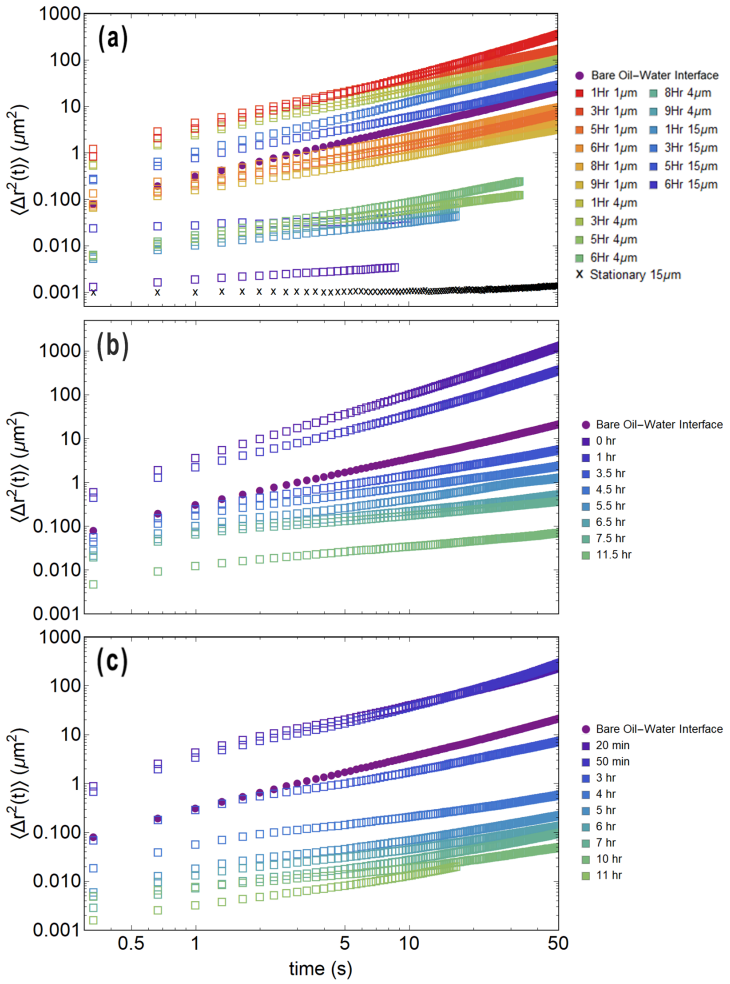

Fig. S1. (a) Mean-squared displacements of 1-μm, 4-μm, and 15-μm-diameter spherical particles at an oil-water interface at various interface ages as indicated in the legend. (b) and (c) Mean-squared displacements of 4-μm-diameter spheres at various interface ages obtained in two additional trials. Also shown in (a) is an estimate of the minimum resolvable ensemble MSD obtained from a measurement on stationary 15-μm spheres.

III. VELOCITY CORRELATIONS OF SPHERICAL COLLOIDS

As further analysis of the sub-diffusive motion of the colloids at late age, we determined the velocity auto-correlation function, defined as

$$C_v^\delta(\tau) = \langle \mathbf{v}^\delta(t'+\tau) \cdot \mathbf{v}^\delta(t') \rangle, \tag{S1}$$

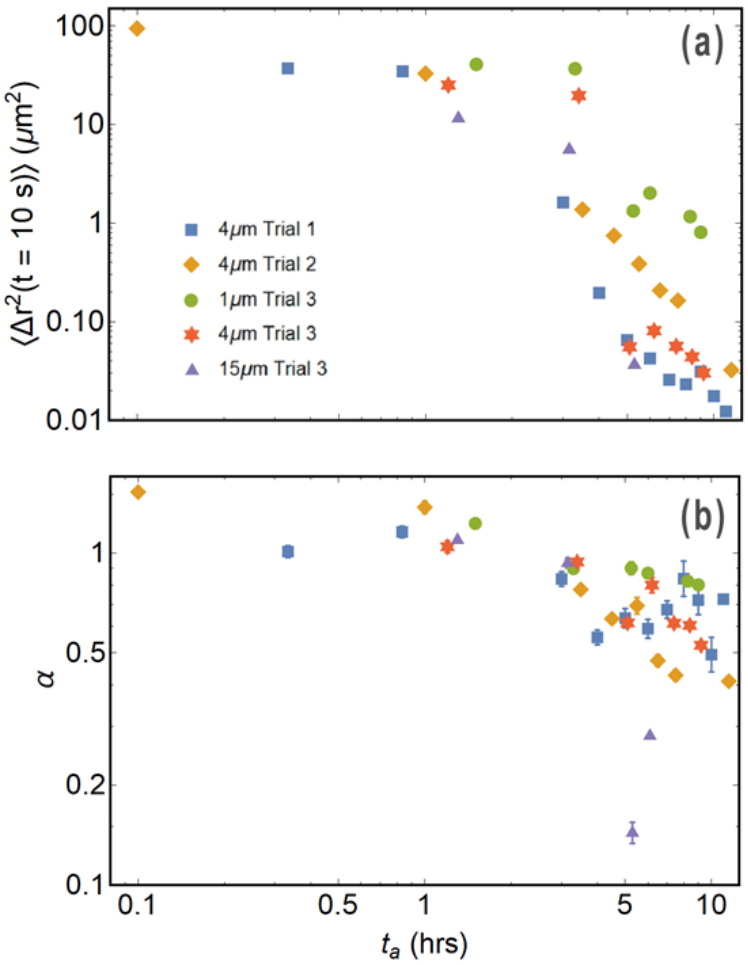

Fig. S2. (a) Values of the MSDs at a lag time of 10 s of spheres of different diameter in three trials, as indicated in the legend, as a function of interface age. (b) Exponents characterizing the power-law behavior of the MSDs.

where the brackets indicate averages over time t' and over particles in the ensemble, and $\mathbf{v}^{\delta}(t')$ is the velocity of a particle averaged over a lag time δ,

$$\mathbf{v}^{\delta}(t') = \frac{1}{\delta}(\mathbf{r}(t'+\delta) - \mathbf{r}(t')) \tag{S2}$$

Figure S3 displays the normalized velocity correlations, $C_v^{\delta}(t)/C_v^{\delta}(0)$ of 4-μm-diameter spheres at an interface age $t_a = 11.5$ hrs for various lag times δ. For comparison, the solid lines in the figure display the normalized velocity correlation functions predicted by a fractional-Brownian-motion model, which is often used to model the motion of particles in viscoelastic materials [1]. Specifically, within this model the predicted velocity correlations

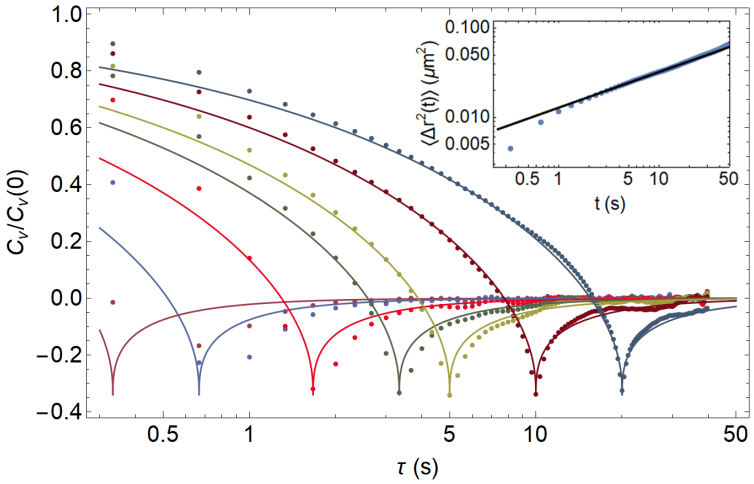

Fig. S3. Normalized velocity correlations of 4-μm-diameter spheres at interface age $t_a = 11.5$ hrs at lag times δ, appearing from left to right, of 1/3, 2/3, 5/3, 10/3, 5, 10, and 20 s. The solid lines show the theoretically predicted normalized correlations based on the fractional-Brownian-motion model [1] with $\alpha = 0.4$, the power-law exponent of the spheres' mean squared displacement, as shown in the inset.

are

$$C_v^{\delta}(\tau) = \begin{cases} \frac{C_v(\tau)}{\kappa^2\alpha(1-\alpha)}2 - (1-\kappa)^{\alpha} - (1+\kappa)^{\alpha}, & \text{for } \tau \geq \delta \\ \frac{C_v(\tau)}{\kappa^2\alpha(1-\alpha)}2 - (1-\kappa)^{\alpha} - (1+\kappa)^{\alpha} + & \\ \frac{3k_BT}{6\pi\alpha\eta}\frac{\sin(\alpha\pi)}{\pi(1-\alpha)(1-\frac{\alpha}{2})\alpha\delta^2}(\delta-\tau)^{\alpha}, & \text{for } \tau < \delta \end{cases} \tag{S3}$$

where $\kappa = \delta/\tau$, α is the power-law exponent of the MSDs, and $C_v(\tau) = \frac{-3k_BT}{6\pi\alpha\eta}\frac{\sin(\alpha\pi)}{\pi(2-\alpha)}|\tau^{\alpha-2}|$. Details regarding the model can be found in [1]. In the calculated correlation functions shown in Fig. S3, the value of α was chosen based on a fit to the ensemble MSD, as shown in the inset to the figure. Therefore, the comparison between the model predictions and the experimental correlation functions is made with no free parameters. The theoretical curves agree well with experimental correlation functions for $\delta \geq 10$. For smaller δ, anti-correlations in the measured velocities ($C_v^{\delta}(\tau) < 0$) persist to longer lag times τ than is predicted by the model.

A. Differential Dynamic Microscopy Analysis Procedure

Differential dynamic microscopy (DDM) analysis was performed on bright-field images acquired at 30 fps with a resolution of 2048×2048 pixels. The analysis resulted in the image structure function $D(q,t)$ at a binned set of wave vectors q and at lag times t. To decrease the calculation time and capture more efficiently the shape of the image structure function, the analysis was performed on exponentially spaced time lags. The analysis typically resulted in approximately 1448 unique values of q and 60 unique lag times. The results were further binned using an exponential spacing of q in order to reduce the computational time in fitting $D(q,t)$. The bin spacing Δq was chosen such that $\Delta q/q$ was approximately 0.1, which was deemed adequate resolution given the lack of sharp features in $D(q,t)$ as a function of q. The range of q was limited to $q = 0.1 - 5.7$ μm^{-1} in order to retain only the statistically most robust $D(q,t)$ with the largest signal-to-noise ratio. Figures S4(a) and (b) display $D(q,t)$ at various wave vectors at $t_a = 1$ hr and 7 hrs, respectively. The results for $1 - g(q,t)$ shown in Fig. 9 of the manuscript were obtained from these data.

As described in the manuscript, a challenge in analyzing the DDM results was to determine whether $g(q,t)$ was ergodic and hence $D(q,t)$ reached a terminal plateau corresponding to $g(q,t) \to 0$. To test whether this condition was met, we conducted a separate DDM analysis on the videos in which subsets of the images were digitally translated, thus ensuring complete decorrelation of the image structure function while maintaining approximately the same structure and noise of the original video. The 800 frames of each video were divided into five sets of 160 images (each set being approximately every 5.3 s in length). The second, third, fourth, and fifth sets were translated digitally with respect to the first set by 300 pixel to the right, left, down, and up, respectively. The choice of 300 pixels, or 83 μm, was made because it was small enough not to appreciably alter the region over which the analysis was performed, while also being large enough to decorrelate the images over length scales greater than q^{-1}, even for the smallest wave vector (0.1 μm^{-1}) included in the analysis. Comparisons of the $D(q,t)$ at $t_a = 1$ hr and 7 hrs obtained with and without this image translation procedure are shown in Fig. S5. The difference in the results at $t_a = 1$ hr is minor, consistent with our assumption that the measurements at early age were ergodic; that is, that $D(q,t)$ reached a terminal plateau corresponding to $g(q,t) \to 0$. However, the difference in results at $t_a = 7$ hrs is more significant, indicating the measurements at later

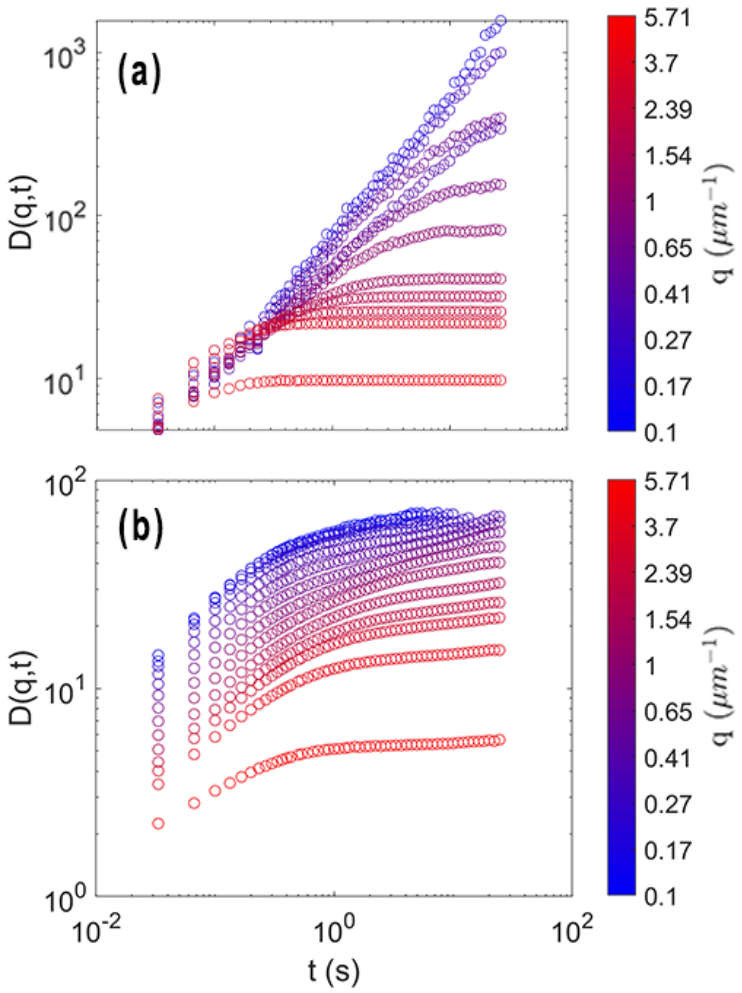

Fig. S4. Image structure functions obtained from a bright-field video of the interface at ages (a) 1 hour and (b) 7 hours. The results for $1 - g(q, t)$ shown in Fig. 9 of the manuscript were derived from these data.

ages were not ergodic. Note $D(q, t)$ at $t_a = 7$ hrs in which the images were shifted shows a sharp kink at $t = 5.3$ s, corresponding the artificially imposed de-correlation. The plateau values of these $D(q, t)$ at greater lag times provided a means to analyze the late-age results.

Since the measurements at $t_a = 1$ hr were apparently ergodic, the data were analyzed accordingly. As described in the main text, $D(q, t)$ at each q was fit using a model of diffusive dynamics for $g(q, t)$,

$$D(q, t) = A(q)(1 - \exp(-t/\tau_D(q))) + B(q) \tag{S4}$$

with $\tau_D(q)$, $A(q)$, and $B(q)$ as free parameters. To obtain initial guesses for each parameter, the following procedure was employed. First, a linear fit to $D(q, t)$ from the analysis with

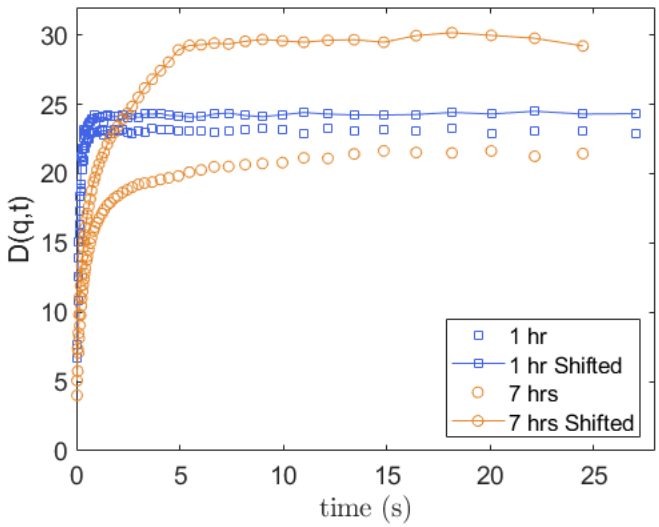

Fig. S5. A comparison of $D(q,t)$ as found from a bright-field video of the interface with that of the same video in which the images were digitally translated. Results are shown at ages of 1 hour (blue squares) and 7 hours (orange circles), at a wave vector of $q = 3\ \mu\text{m}^{-1}$. The video in which the frames were artificially translated produces a plateau in $D(q,t)$ at lag times that are greater than the interval between translations, which is approximately 5.3 seconds. The large difference in $D(q,t)$ between the translated and original videos at 7 hours, compared to the negligible difference between the two at 1 hour, indicates a lack of complete decay of the ISF at the later age.

artificial shifts was performed using the data at small lag times, and the y-intercepts of those fits were used as the initial guesses for $B(q)$. Then, the differences between the large-lag-time plateaus of $D(q,t)$ from the analysis with artificial shifts and these y-intercepts values were obtained, and these were used as the initial estimates of $A(q)$. The estimates are shown in Fig. S6 as $A_0(q)$ and $B_0(q)$. Finally, initial guesses for $\tau(q)$ at $t_a = 1$ hr were made by assuming $\tau_D \sim q^{-2}$. In the fitting, $A(q)$, $B(q)$, and $\tau(q)$ were all constrained to be greater than zero, and $A(q)$ was also constrained to be less than 10^4 to help the fits converge. The final results for $\tau_D(q)$ are shown in Fig. 10 of the manuscript. Figure S6 shows the final results for $A(q)$ and $B(q)$.

The large discrepancy at $t_a = 7$ hrs between $D(q,t)$ obtained with and without artificially de-correlating the images indicates the measurements were not ergodic at this age; that is, $g(q,t)$ failed to decay fully to zero over the range of measured lag times. In such cases,

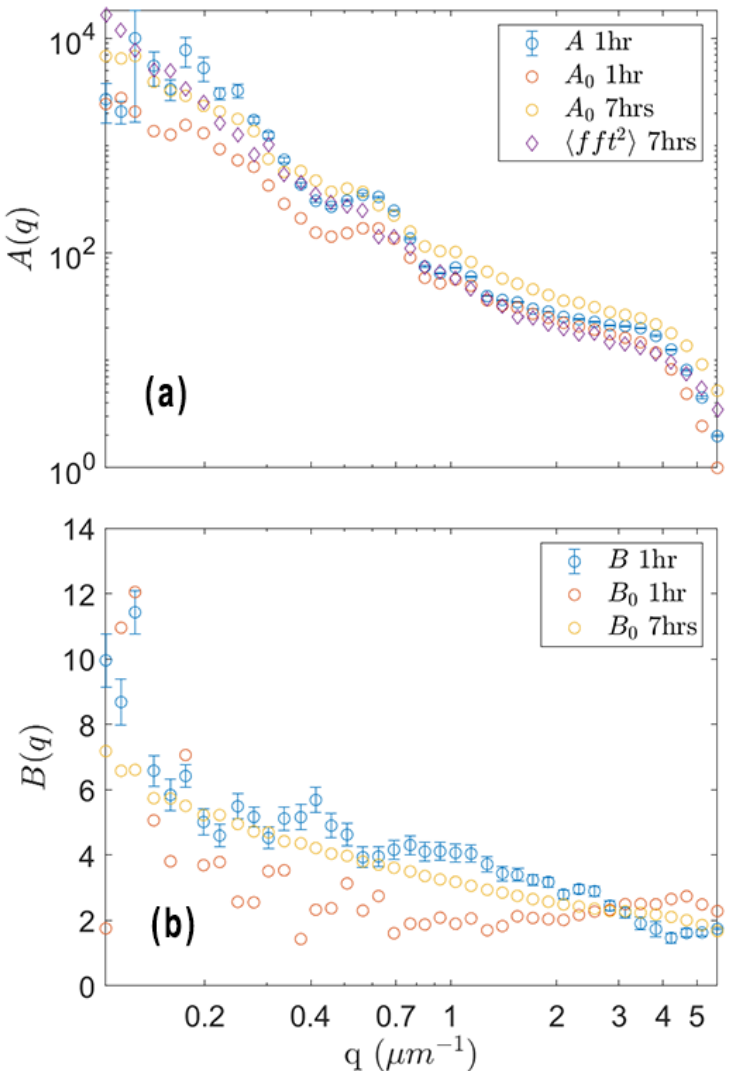

Fig. S6. The parameters $A(q)$ and $B(q)$ at interface ages of 1 and 7 hours. (a) The scaling parameter $A(q)$, as found from the exponential fits to the data at an age of 1 hour, along with $A_0(q)$ the plateau of $D(q,t)$ found from the digitally translated frames at both an age of 1 and 7 hours. Also shown is the average squared fast Fourier transform of the bright-field images at 7 hours. (b) The value of $B(q)$ found from the fits at 1 hour and $B_0(q)$, the initial estimate at 1 and 7 hours.

one cannot directly obtain a reliable estimate of $D(q,t)$ on an absolute scale. Therefore, from $D(q,t)$ of the artificially shifted data, we obtained values of $A(q)$ and $B(q)$ that we used in the analysis of the results from the unaltered images. Specifically, we followed the same procedure we employed to obtain initial guesses for $A(q)$ and $B(q)$ at $t_a = 1$ hr, but in this case we kept those values fixed in the subsequent analysis. These values for $A(q)$

and $B(q)$ at $t_a = 7$ hrs are shown in Fig. S6. As a cross-check, also shown in Fig. S6(a) is the squared Fourier transform of the bright-field images at $t_a = 7$ hrs averaged over the video. One can show that the averaged squared Fourier transform is proportional to $A(q)$, and indeed our estimate of $A(q)$ demonstrates this well. Notably, we find little qualitative difference between the average Fourier transform of the images at 1 and 7 hours. Therefore, the similarity of $A(q)$ between these two ages is also reasonable.

With $A(q)$ and $B(q)$ fixed in this way, we fit each $D(q,t)$ at $t_a = 7$ hrs using Eq. (15) in the main text, allowing τ_1, τ_2, λ, and α to vary with the constraint that all parameters must be greater than zero. We also constrained τ_2 to be less than 0.1 s to prevent the algorithm from incorporating it too strongly into the fit, as it is merely included to keep the modeled image structure function physical. Although on several occasions τ_2 reached the maximum value allowed by the constraint, we found that the fit result was largely insensitive to its precise value.

---

[1] S. C. Weber, A. J. Spakowitz, and J. A. Theriot, Bacterial chromosomal loci move subdiffusively through a viscoelastic cytoplasm, Phys. Rev. Lett. **104**, 238102 (2010).

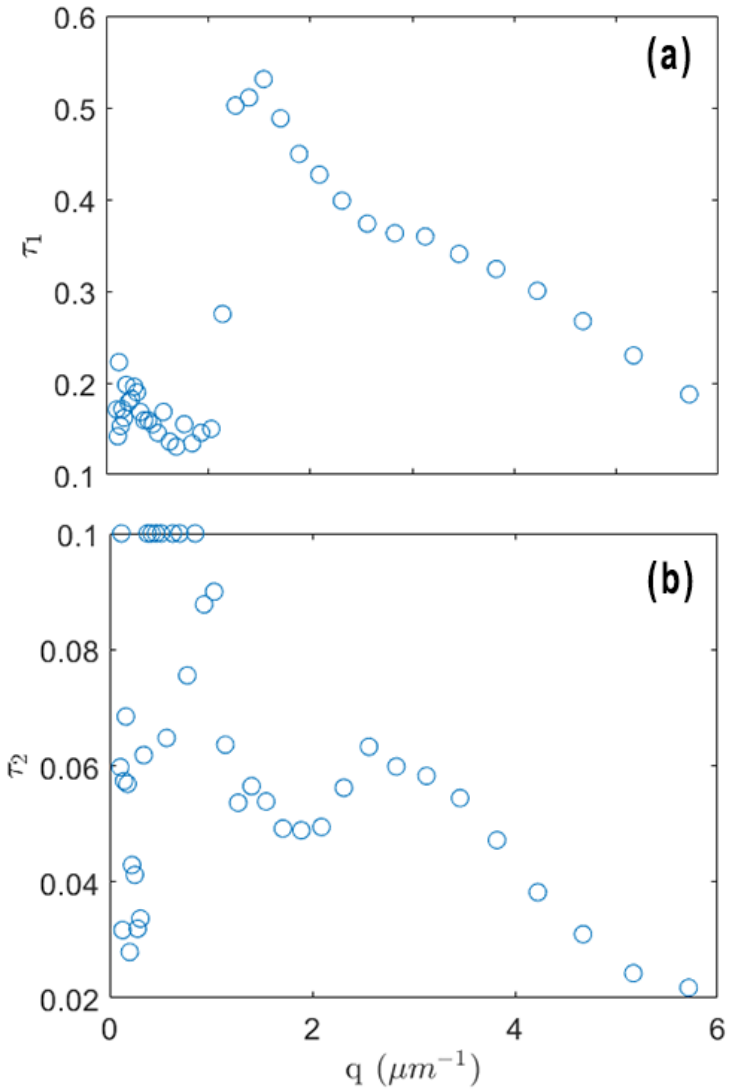

Fig. S7. The fit parameters τ_1 (a) and τ_2 (b) found from fits to $D(q,t)$ at an age of 7 hours, as explained in the main text.